



Teanby, N. A., Irwin, P. G. J., Nixon, C. A., Courtin, R., Swinyard, B. M., Moreno, R., Lellouch, E., Rengel, M., & Hartogh, P. (2013). Constraints on Titan's middle atmosphere ammonia abundance from Herschel/SPIRE sub-millimetre spectra. *Planetary and Space Science*, 75, 136-147. <https://doi.org/10.1016/j.pss.2012.11.008>

Peer reviewed version

Link to published version (if available):
[10.1016/j.pss.2012.11.008](https://doi.org/10.1016/j.pss.2012.11.008)

[Link to publication record in Explore Bristol Research](#)
PDF-document

University of Bristol - Explore Bristol Research

General rights

This document is made available in accordance with publisher policies. Please cite only the published version using the reference above. Full terms of use are available:
<http://www.bristol.ac.uk/red/research-policy/pure/user-guides/ebr-terms/>

Constraints on Titan’s middle atmosphere ammonia abundance from Herschel/SPIRE sub-millimetre spectra[☆]

N. A. Teanby^a, P. G. J. Irwin^b, C. A. Nixon^c, R. Courtin^d, B. M. Swinyard^{e,f}, R. Moreno^d, E. Lellouch^d, M. Rengel^g, P. Hartogh^g

^a*School of Earth Sciences, University of Bristol, Wills Memorial Building, Queen’s Road, Bristol, BS8 1RJ, U.K.*

^b*Atmospheric, Oceanic & Planetary Physics, Department of Physics, University of Oxford, Clarendon Laboratory, Parks Road, Oxford, OX1 3PU. UK.*

^c*NASA Goddard Space Flight Center, Greenbelt, Maryland, USA.*

^d*LESIA-Observatoire de Paris, CNRS, Université Paris 6, Université Paris-Diderot, 5 place Jules Janssen, 92195 Meudon, France*

^e*RAL Space, Science & Technology Facilities Council, Rutherford Appleton Laboratory, Chilton, Didcot, OX11 0QX, UK.*

^f*Physics and Astronomy Department, University College London, Gower Street, London, WC1E 6BT, UK.*

^g*Max-Planck-Institut für Sonnensystemforschung, Max-Planck-Str. 2, 37191 Katlenburg-Lindau, Germany*

Abstract

Sub-millimetre spectra measured with Herschel’s SPIRE Fourier Transform Spectrometer were used to search for ammonia (NH₃) in Titan’s stratosphere. Observations were taken during 2010 and 2011, just after Titan’s northern spring equinox, which occurred in mid-2009. In our analysis we used high spectral resolution data (0.074 cm^{−1} apodised) from the SPIRE shortwave spectrometer array (SSW), which provided the best possible signal-to-noise ratio for detecting any NH₃ emission features. These data have the most

[☆]*Herschel* is an ESA space observatory with science instruments provided by European-led Principal Investigator consortia and with important participation from NASA.

Email address: n.teanby@bristol.ac.uk (N. A. Teanby)

sensitivity to NH_3 spectral emission of any currently available observations, although despite this we did not detect any significant emission features above the noise. However, we can place an improved 3-sigma upper limit on NH_3 abundance of <0.19 ppb for altitudes 65–110 km (75 km peak sensitivity), or alternatively a column abundance of $<1.23 \times 10^{15}$ molecules/cm². These observations provide modest constraint for future photochemical models and are consistent with most current stratospheric predictions. Scaling of photochemical model profiles, in order to fit elevated abundances observed at 1100 km by Cassini’s INMS instrument, are for the most part also consistent with our observations.

Keywords: Titan, Atmosphere, Composition, Photochemistry, Herschel, sub-millimetre

1. Introduction

Titan, Saturn’s largest moon, is unusual because it has a thick nitrogen and methane atmosphere (1.5 bar surface pressure). Interaction with solar UV photons and magnetospheric electrons in Titan’s upper atmosphere creates nitrogen and methane radicals, which form the basis of a rich photochemical cycle - producing a vast array of hydrocarbon and nitrile species (Wilson and Atreya, 2004; Lavvas et al., 2008; Krasnopolsky, 2009). These photochemical processes lead to the creation of complex organic molecules.

An essential element in understanding Titan’s complex atmosphere is accurate measurement of trace species abundances at different atmospheric levels, which provide stringent constraints on active chemical pathways. Recently the Cassini-Huygens mission has played a critical role in unlocking the

13 complexity of Titan’s chemical inventory. Many new compounds have been
14 discovered in the very upper layers of the atmosphere (>950 km altitude)
15 using Cassini’s Ion and Neutral Mass Spectrometer (INMS) (Waite et al.,
16 2005; Vuitton et al., 2009), which samples gas for *in situ* analysis on each
17 close flyby.

18 Deep within Titan’s atmosphere, in the stratosphere and mesosphere
19 (100–500 km altitude), remote sensing techniques currently provide the most
20 complete information on atmospheric composition. For example, in the sub-
21 millimetre, recent Herschel observations have lead to the discovery of HNC
22 (Moreno et al., 2011), abundance determinations of CO, HCN and their iso-
23 topologues (Courtin et al., 2011), and water vapour vertical profiles (Moreno
24 et al., 2012). At shorter wavelengths, in the far- and mid-infrared, which con-
25 tain many more gas emission features, Cassini’s Composite InfraRed Spec-
26 trometer (CIRS) has been very successful at measuring the detailed altitude
27 and latitude distribution of major trace species (Flasar et al., 2005; Couste-
28 nis et al., 2007, 2010; de Kok et al., 2007a; Nixon et al., 2009; Teanby et al.,
29 2006b, 2007, 2008a,b, 2009b,a, 2010a; Vinatier et al., 2007, 2010; Cottini
30 et al., 2012). However, the CIRS spectral resolution and sensitivity has so far
31 been too low to detect emission features from any of the new species discov-
32 ered at much higher altitudes by INMS. See for example Nixon et al. (2010)
33 who used CIRS to determine upper limits for H_2CO , CH_3OH , CH_3CN , C_3H_4
34 (allene isomer), and NH_3 . The abundance of many important molecules,
35 including NH_3 , are thus currently unconstrained in the middle atmosphere.

36 To further our understanding of Titan’s atmosphere it is now critical to
37 link the chemistry of the upper atmosphere (above 1000 km) to that of the

38 stratosphere and mesosphere (100–500 km), which contain the majority of
 39 Titan’s trace gas inventory. One of the key molecules for providing this link
 40 is ammonia (NH_3), which was measured with a volume mixing ratio (VMR)
 41 of 7×10^{-6} by INMS at 1100 km (Vuitton et al., 2007; Vuitton et al., 2009). A
 42 major deficiency of current chemical schemes is that the NH_3 abundance at
 43 this altitude is underestimated by orders of magnitude: Wilson and Atreya
 44 (2004) predict 4×10^{-8} at 1100km (175 times less the observed); and Lavvas
 45 et al. (2008) and Krasnopolsky (2009) both predict around 2×10^{-7} at 1100km
 46 (35 times less). Therefore, the mechanism for NH_3 production in Titan’s
 47 atmosphere would appear to be much more efficient than current schemes
 48 can explain.

49 Current photochemical models produce high altitude (1100 km) NH_3 by
 50 electron recombination with NH_4^+ ions. However, recently Yelle et al. (2010)
 51 hypothesised that disagreement between models and the INMS observations
 52 could be caused by a previously neglected NH_3 production pathway: $\text{NH}_2 +$
 53 $\text{H}_2\text{CN} \rightarrow \text{NH}_3 + \text{HCN}$, which they propose is the dominant NH_3 source at
 54 high altitude.

55 In the stratosphere and mesosphere NH_3 is expected to be supplied via
 56 transport from high altitudes by vertical mixing processes. Hence, increased
 57 production at higher altitude should imply an increase in NH_3 at lower at-
 58 mospheric levels also, which can be searched for using NH_3 sub-millimetre
 59 emission lines. There is also a possible local stratospheric source of NH_3 from
 60 cosmic ray induced dissociation of molecular nitrogen, which could lead to a
 61 local maximum in NH_3 abundance in the stratosphere (see e.g. Lavvas et al.
 62 (2008)). Measurements of C_2N_2 (Teanby et al., 2009a) suggest that cosmic

63 rays may indeed play an important role in Titan’s stratospheric chemistry.
64 However, stratospheric and mesospheric predictions of NH_3 abundance from
65 the different published models vary by over two orders of magnitude and are
66 not well constrained by current observations.

67 NH_3 has so far not been observed spectroscopically at all, and the best
68 previously available stratospheric upper limit of 1.3×10^{-9} (Nixon et al., 2010)
69 is too large to differentiate between possible photochemical models, which
70 currently predict relative stratospheric abundances of order 10^{-10} or less (e.g.
71 Lavvas et al., 2008). In this paper we use high sensitivity sub-millimetre
72 observations by Herschel’s SPIRE Fourier Transform Spectrometer (FTS)
73 instrument to search for NH_3 in Titan’s lower stratosphere in an attempt to
74 provide improved constraints on photochemical pathways.

75 2. Observations

76 Observations were taken with the Herschel Space Observatory’s (Pilbratt
77 et al., 2010) SPIRE instrument (Griffin et al., 2010) as part of the HssO Key
78 Program (Hartogh et al., 2009), just after Titan’s mid-2009 northern spring
79 equinox, between 22/6/2010 and 26/07/2011. The SPIRE FTS simultane-
80 ously observes a full spectrum from 14.6 to 51.8 cm^{-1} (685 – $193 \text{ }\mu\text{m}$) using
81 two separate detector arrays to ensure maximum observing efficiency. The
82 shortwave spectrometer array (SSW) covers 31.2 – 51.8 cm^{-1} and the long-
83 wave spectrometer array (SLW) covers 14.6 – 33.3 cm^{-1} . Observations were
84 taken in high spectral resolution sparse pointed mode whereby the object is
85 detected only in the central detector of each array and the whole spectrum
86 is taken with a single spectral resolution. The nature of the detector spa-

87 tial sampling, combined with Herschel’s 3.5 m primary mirror, resulted in
 88 wavelength-dependent individual detector field-of-views of diameter 11–19”
 89 for the SSW and 18–40” for the SLW (Swinyard et al., 2010). Titan’s disc
 90 typically had a solid-body diameter of 0.7” during these observations, result-
 91 ing in disc-averaged spectra. The SSW spectra have the best signal-to-noise
 92 for our study as they cover the strongest NH_3 lines and have the least beam
 93 dilution because of their smaller field-of-view (FOV). It is these observations
 94 we concentrate on here. The SPIRE point observing mode sequences had
 95 total integrations between 22 minutes and 8 hours 51 minutes. The total in-
 96 tegration time was built up from multiple scans of the FTS mechanism, with
 97 each scan taking approximately 66 seconds. Following transformation to the
 98 spectral domain, the integrated spectrum from each observation sequence
 99 was formed by co-addition of the individual spectra. Observation properties
 100 are listed in Table 1. Five observations were taken in total, but we only
 101 use four of these in this paper - the first observation is not used because of
 102 its short integration time and contamination from Saturn. Figure 1 shows
 103 the observing geometry and Titan’s orientation during the four observation
 104 sequences.

105 Our analysis started with unapodised Level 2 data from the Herschel Sci-
 106 ence Archive (HSA), which are calibrated against the continuum spectrum of
 107 Uranus (Swinyard et al., 2010). Data had a sample spacing of 0.01 cm^{-1} and
 108 a native resolution comprising a sinc instrument function with a full-width
 109 half-maximum (FWHM) of 0.048 cm^{-1} . These data were apodised using a
 110 Hamming instrument function with a FWHM of 0.07373 cm^{-1} to remove the
 111 effects of ringing around gas emission peaks. This choice provided the best

112 compromise between reducing ringing and maintaining the narrow widths of
 113 gas peaks. Apodised spectra (Figure 2) show a very clean signal with min-
 114 imal noise features, although some slight continuum ripples are present due
 115 to residual instrumental effects. Initially we used the nominal error bar from
 116 the HSA, which was calculated using the standard deviation of the multiple
 117 scans taken to build up the total integrated spectrum. These errors were
 118 further refined during the analysis (Section 3.5).

119 **3. Modelling and further data reduction**

120 Our study is focussed on searching for very faint NH_3 spectral lines.
 121 Therefore, our main concern is defining realistic error bars and achieving
 122 an accurate continuum level so that any small features can be identified.
 123 The observed spectra contain superimposed ripples, which are instrument
 124 artifacts and not associated with Titan’s spectrum. These must be removed
 125 before analysis can proceed. Commonly such artifacts are dealt with by
 126 modelling the line-to-continuum ratio. However, in this paper we chose to
 127 preserve the physical radiance units, which has the advantage of providing
 128 an additional check on the data calibration and model accuracy, in addition
 129 to being more intuitive to analyse.

130 In the wavelength region covered by the SSW, Titan’s spectrum is af-
 131 fected by tropopause and lower stratospheric temperature, collision-induced
 132 absorption of $\text{N}_2\text{-CH}_4\text{-H}_2$ pair combinations, emission lines from isotopo-
 133 logues of CO, HCN, and to a lesser extent CH_4 , and minimally by strato-
 134 spheric haze. All these properties are well constrained by the Cassini CIRS
 135 instrument (Flasar et al., 2004, 2005) and the Huygens descent probe HASI

136 (Fulchignoni et al., 2005) and GCMS instruments (Niemann et al., 2010),
 137 allowing a reliable synthetic spectrum to be generated for comparison with
 138 the SPIRE observations.

139 The aim of the remainder of this section is to use realistic baseline syn-
 140 thetic reference spectra to identify and remove ripples, leaving a cleaned
 141 spectrum suitable for identification of any small NH_3 features. This proce-
 142 dure comprises the following steps:

143 *3.1. Conversion of radiance units*

144 Spectra from the SPIRE Level 2 calibration pipeline have units of Janskys
 145 - the natural unit for unresolved point sources (Wilson et al., 2009) - where
 146 $1 \text{ Jy} = 10^{-26} \text{ W/m}^2/\text{Hz}$. However, to correctly model Titan's disc-averaged
 147 spectra and account for varying emission angle, it is necessary to consider the
 148 spatial distribution of radiance, so units of spectral radiance $\text{W/cm}^2/\text{sr/cm}^{-1}$
 149 are a more convenient working unit. To convert between the two units we
 150 must define the solid angle over which the emission takes place. For a solid
 151 body this would be simply defined from the cross sectional area of the object.
 152 However, emission from the limb of Titan's extended atmosphere is significant
 153 well above its solid surface. This emission can be assumed to drop to zero at a
 154 radius of 3000 km for sub-millimetre wavelengths (Appendix A). Therefore,
 155 to obtain a disc-averaged spectral radiance, we assumed uniform emission
 156 over a circular area centred on Titan, with a radius of $r=3000\text{km}$. The exact
 157 choice of r is not critical so long as it is large enough to include all of Titan's
 158 emission.

159 Consider a planet emitting over a circular area of radius r , a distance R

160 from the observer. The solid angle Ω subtended by the planet is given by

$$\Omega = \pi \frac{r^2}{R^2} \quad (1)$$

161 Dividing Janskys by Ω gives us units of spectral radiance $10^{-26} \text{W/m}^2/\text{sr/Hz}$
 162 To convert these units to the more standard $\text{W/cm}^2/\text{sr/cm}^{-1}$ we must mul-
 163 tiply by $10^{-26} \times c \times 10^{-4}$, where $c = 2.99792458 \times 10^{10} \text{ cm/s}$ is the speed
 164 of light - 10^{-26} converts into Watts, 10^{-4} converts m^{-2} into cm^{-2} , and c
 165 converts frequency to wavelength.

166 The overall conversion is thus:

$$1\text{Jy} = 10^{-30} \frac{cR^2}{\pi r^2} \text{W/cm}^2/\text{sr/cm}^{-1} \quad (2)$$

167 3.2. Forward modelling of the SSW spectra

168 Synthetic reference spectra were created using the Nemesis retrieval tool
 169 (Irwin et al., 2008), which assumes a spherically symmetric atmosphere and
 170 uses the correlated-k approximation (Lacis and Oinas, 1991) for computa-
 171 tional efficiency. Previously, we have used this code extensively to model
 172 Titan’s spectrum (e.g. Teanby et al., 2010c, and references therein).

173 Gas spectroscopic data were based on the HITRAN database (Rothman
 174 et al., 2005) with the following modifications: CH_4 line intensities were re-
 175 visited after Wishnow et al. (2007); and HCN linewidths were modified for
 176 N_2 broadening as explained in Teanby et al. (2010b). Tables of absorption
 177 coefficients - or k-tables - were created from the spectroscopic data and in-
 178 corporated the Hamming instrument function directly in order to improve
 179 computational efficiency and to provide the best match to observations. The
 180 partition functions were calculated using a third order polynomial fit to the

181 total partition function data in Fischer et al. (2003) (supplied with the HI-
 182 TRAN database) over the range 70–300 K. Collision-induced absorption from
 183 pairwise combinations of N₂, CH₄, and H₂ were calculated according to Bo-
 184 rysow and Frommhold (1986a,b,c, 1987); Borysow (1991); Borysow and Tang
 185 (1993). The wavenumber dependence of the main haze relative absorption
 186 cross section was determined from the volume absorption coefficients in An-
 187 derson and Samuelson (2011). The values we used are given in Table 2.

188 A reference atmosphere was then defined with composition, aerosol, and
 189 temperature profiles based on previous work. The assumed haze vertical pro-
 190 file was a simplified version based on results from CIRS (de Kok et al., 2007b,
 191 2010) and Huygens/DISR (Tomasko et al., 2008) (Figure 6). This profile was
 192 scaled such that the specific particle density was 3.9×10^{-2} particles/gram at
 193 150 km. This scaling gave a specific absorption of 3.9×10^{-2} particles/gram
 194 $\times 1.26 \times 10^{-3} \text{ cm}^2/\text{particle} = 4.9 \times 10^{-5} \text{ cm}^2/\text{gram}$ for an altitude of 150 km
 195 at 160 cm^{-1} , in agreement with Anderson and Samuelson (2011) (their Fig.
 196 10 at latitude 15°S). The calculated nadir optical depth using this profile at
 197 the centre of the SSW bandpass (42 cm^{-1}) was 2.4×10^{-3} (see also Table 2).
 198 For comparison, Titan’s atmosphere is effectively opaque at these wavenum-
 199 bers due to N₂-N₂ and N₂-CH₄ collision-induced absorption, with an optical
 200 depth of unity occurring around 50 km altitude. Therefore, aerosols have
 201 very slight influence on this spectral region, but were included for complete-
 202 ness. The atmospheric temperature profile was based on Flasar et al. (2005)
 203 (Figure 6) and gas vertical profiles were based on: Niemann et al. (2010)
 204 (CH₄); de Kok et al. (2007a) (CO); and Teanby et al. (2010b) (HCN). These
 205 values can be considered representative of equatorial conditions at the time

206 of our observations.

207 After defining the spectroscopic parameters and reference atmosphere
208 we calculated a Titan reference spectrum. To allow for differing emission
209 angles and limb emission across Titan’s disc, we created a disc-averaged
210 spectrum based on 21 field-of-view points (Teanby and Irwin, 2007) using
211 the procedure outlined in Appendix A. This is directly comparable to the
212 unit-converted spectra from Section 3.1. Figure 3a shows observation S1
213 compared to the reference atmosphere synthetic. The agreement is very
214 close and gives us confidence in both the Level 2 data calibration and forward
215 model. The model was also cross-checked against an independent radiative
216 transfer code (Courtin et al., 2011). Note the reference synthetic spectrum is
217 based entirely on prior knowledge from Cassini and at this point is not fitted
218 to the observations in any way.

219 3.3. Removal of continuum ripples

220 The close agreement between observed and reference synthetic spectra
221 allows us to correct for continuum ripples by making minor adjustments
222 to the observed radiances based on the residual between the two spectra.
223 However, the gas peaks contain real differences due to unmodelled spatial
224 variations in temperature and composition over Titan’s globe. Therefore,
225 before estimating the continuum ripples the gas peaks must be masked out.
226 To create a spectral mask we created a second reference spectrum with HCN,
227 CO, and CH₄ rotational emission lines removed, and differenced this with the
228 original reference spectrum. Any wavenumbers where the two spectra differed
229 by more than 0.1 nW/cm²/sr/cm⁻¹ were considered to be influenced by
230 HCN/CO/CH₄ emission and were masked out. Figure 3b shows the reference

spectra with gas peaks masked out - this allows the continuum ripples to be seen very clearly. Figure 3c shows the residuals between observation and masked reference spectra, which has an amplitude of a few $\text{nW}/\text{cm}^2/\text{sr}/\text{cm}^{-1}$.

To use the residuals to remove the ripples we must first apply some smoothing and interpolation to: i) allow correction of the continuum where gas lines exist; and ii) to avoid removing any narrow gas features from unmodelled trace species such as NH_3 . To this end we fit a cubic b-spline curve with a knot spacing of 1.25 cm^{-1} (total spline width of 5 cm^{-1}) using the method of Teanby (2007) and remove this smoothed continuum residual from the observed spectra. Narrow gas lines will be unaffected by this procedure but if any real unmodelled broad features exist in the measurements they will be removed. This is unlikely, and in any case is not important for our purposes as any gas lines are much narrower than the knot spacing. The final ripple corrected spectrum is shown in Figure 3d. As the ripple position and amplitude changed for each observation, this process was performed individually for each of the four observed spectra.

3.4. *Correction of wavelength scale*

While modelling the spectra it was noticed that slight sub-sample scale wavenumber shifts existed in the observations. While small, these were very noticeable around the sharp gas peaks of HCN and CO. To correct for this, the reference synthetic spectrum was cross correlated with each observation to determine the shift magnitude and direction. The wavenumber grid was then shifted and the resulting spectrum linearly interpolated back onto the original wavenumber grid. Oversampling of the spectra was sufficiently fine that this did not introduce any interpolation artifacts (for example reduced

256 peak heights). Shifts were all less than 0.005 cm^{-1} (Table 1) which is small
 257 compared to the 0.01 cm^{-1} sample spacing.

258 3.5. Creation of a final averaged spectrum

259 To maximise the signal-to-noise an average spectrum was created from
 260 the four individual de-rippled and wavelength corrected spectra S1–S4. This
 261 gave us an opportunity to improve the noise estimate on the spectrum using
 262 the standard deviation $\delta(\nu_j)$ between the four measured spectra $s_i(\nu_j)$ at
 263 wavenumbers ν_j . Due to the small number of spectra, $\delta(\nu_j)$ will suffer from
 264 small number statistics and could be anomalously small, giving an unreal-
 265 istically low value of the error for some wavenumbers. Therefore, to obtain
 266 a more accurate noise estimate, which can be used as a minimum measure-
 267 ment error at each wavenumber, we assume that the standard deviation is
 268 uniform across the whole spectral range. The standard deviation from all
 269 wavenumbers then provides a large number of independent estimates of the
 270 actual standard deviation, which can be combined to determine the sample
 271 mean standard deviation $\bar{\mu}$.

272 As standard deviation is restricted to positive numbers, the estimates
 273 $\delta(\nu_j)$ of $\bar{\mu}$ should be distributed log-normally (Forbes et al., 2011). In such a
 274 distribution the logarithm of the quantity is distributed normally and $\bar{\mu}$ can
 275 be estimated as follows.

276 Consider $M = 4$ measured spectra $s_i(\nu_j)$ where $i = 1 \dots M$ at N wavenum-
 277 bers $\nu_j = 1 \dots N$. The mean $\bar{s}(\nu_j)$ and standard deviation $\delta(\nu_j)$ at each
 278 wavenumber ν_j are given by the usual equations for unweighted sample mean
 279 and standard deviation:

$$\bar{s}(\nu_j) = \frac{\sum_{i=1}^M s_i(\nu_j)}{M} \quad (3)$$

$$\delta(\nu_j) = \sqrt{\frac{\sum_{i=1}^M (s_i(\nu_j) - \bar{s}(\nu_j))^2}{M-1}} \quad (4)$$

280 If $\delta(\nu_j)$ is distributed log-normally, the cumulative distribution function
 281 (CDF) is given by:

$$P(\delta \leq x | \mu, \sigma) = \frac{1}{\sigma\sqrt{2\pi}} \int_0^x \frac{\exp(-(\ln t - \mu)^2 / 2\sigma^2)}{t} dt \quad (5)$$

282 where t is a dummy variable, and μ and σ are the mean and standard devi-
 283 ation of the logged distribution $\ln \delta$ (Forbes et al., 2011). The corresponding
 284 mean $\bar{\mu}$ of the un-logged distribution is given by:

$$\bar{\mu} = \exp\left(\mu + \frac{\sigma^2}{2}\right) \quad (6)$$

285 Parameters μ and σ of the log-normal distribution can be trivially cal-
 286 culated from the N values of $\ln \delta(\nu_j)$, and the equivalent mean standard
 287 deviation $\bar{\mu}$ calculated. If $\bar{\mu}$ is representative of the continuum standard de-
 288 viation, then there should be good correspondence between observed and
 289 theoretical cumulative distribution function (CDF). Figure 4a shows the dis-
 290 tribution of standard deviation estimates $\delta(\nu_j)$ for the entire spectral range,
 291 along with the theoretical distribution calculated using Equation (5) and
 292 (6). This exhibits a mismatch between measured and theoretical log-normal
 293 CDFs, which is caused by a tail of high standard deviations. Inspection of
 294 the data showed that standard deviations of wavenumbers centred on the

295 gas peaks were higher than those in the continuum regions. This is to be
 296 expected, as the slight differences in viewing geometry between observations
 297 cause more of the cold north polar region to come into view during later
 298 observations, which gives rise to systematic differences between the spectral
 299 peaks. Seasonal variations in Titan's atmosphere (Teanby et al., 2010c) could
 300 also have an effect. However, if the gas peaks are masked out, the agreement
 301 with the theoretical distribution is very good (Figure 4b) - with $\bar{\mu}$ providing
 302 a reliable estimate of the actual continuum standard deviation. Therefore,
 303 as an overall conservative error estimate, we set a minimum standard deviation
 304 of $\bar{\mu}=0.26$ nW/cm²/sr/cm⁻¹ on the final combined average spectrum, in
 305 keeping with the estimate derived from continuum points, but if the calculated
 306 standard deviation for a particular wavenumber was larger than this,
 307 we used the larger value - i.e. the final error bar $\bar{\sigma}(\nu_j) = \max(\bar{\mu}, \delta(\nu_j))$

308 The final averaged spectrum $\bar{s}(\nu_i)$ and error bar $\bar{\sigma}(\nu_i)$ are shown in Figure 5
 309 and is composed of the unweighted average of four SPIRE spectra that
 310 have each individually had ripples removed and been corrected for any slight
 311 wavenumber shifts. This final cleaned spectrum was used to determine a
 312 baseline model most appropriate for the disc-averaged spectra. The fit was
 313 obtained by adjusting HCN and CO abundance such that the misfit between
 314 data and synthetic was minimised. Optimal values of HCN and CO were
 315 140 ± 20 ppb and 47 ± 7 ppm respectively. CO abundance is consistent with
 316 previous disc-averaged CO results of 40 ± 5 ppm (Courtin et al., 2011) and
 317 space based determinations from CIRS of 47 ± 8 ppm (de Kok et al., 2007a)
 318 and 55 ± 6 ppm (Teanby et al., 2010b). HCN is spatially highly variable, but
 319 results are consistent with disc-resolved CIRS measurements that indicate

320 abundances of 100–300 ppb at tropical latitudes (Teanby et al., 2010b). The
 321 agreement of our disc-averaged results with previous spatially resolved de-
 322 terminations from CIRS shows that our assumption of spherically symmetry
 323 has not adversely affected the composition results.

324 4. Calculation of upper limits

325 The averaged spectrum from the previous section forms the basis of our
 326 upper limit calculations. The misfit χ^2 between measured and modelled
 327 spectra for a given NH_3 abundance α is given by:

$$\chi^2(\alpha) = \frac{\sum_{i=1}^N (\bar{s}(\nu_i) - f(\nu_i, \alpha))^2}{\bar{\sigma}^2(\nu_i)} \quad (7)$$

328 where $\bar{s}(\nu_i)$ is the measured spectrum with variance $\bar{\sigma}^2(\nu_i)$, and $f(\nu_i, \alpha)$
 329 is the modelled spectrum. First, we take the best fitting model from the
 330 previous section and calculate the initial misfit $\chi^2(0)$. Second, we introduce
 331 a gradually increasing volume mixing ratio (VMR) of ammonia α to calculate
 332 the function $\chi^2(\alpha)$. If NH_3 emission features exist in the spectrum, the fit
 333 should be improved and $\chi^2(\alpha)$ will have a significant minimum at the best
 334 fitting abundance. If insufficient NH_3 is present to produce a detectable
 335 feature then no significant minimum will exist and $\chi^2(\alpha)$ will increase. As
 336 we are adjusting a single variable (the NH_3 abundance), a 3-sigma upper limit
 337 would usually be defined as the point where χ^2 has increased by $3^2 = 9$ (Press
 338 et al., 1992). However, because the spectrum is oversampled by a factor of
 339 four, there is only one independent data point for every four. Therefore,
 340 the 3-sigma upper limit is defined when $\chi^2(\alpha)$ increases by $3^2 * \sqrt{4} = 18$ to
 341 $\chi^2(\alpha) = \chi^2(0) + 18$. Similarly, a 3-sigma detection would require a reduction

342 in $\chi^2(\alpha)$ of 18 to $\chi^2(\alpha) = \chi^2(0) - 18$. Except for this modification for
 343 oversampling, this method is the same as Teanby et al. (2006a, 2009a).

344 The size of NH_3 spectral feature is somewhat dependent on the NH_3
 345 vertical profile as well as its abundance. As this is currently unknown we
 346 explore two end member cases:

- 347 • **Uniform profile:** Where the volume mixing ratio is constant above
 348 the condensation level. Below the condensation level it is defined by the
 349 saturation vapour pressure, which at temperature T in Kelvin is given
 350 in atmospheres by $P_{svp}(T) = \exp(A + B/T + CT)$ with $A=22.70358$,
 351 $B=-4190.773$ K, $C=-0.2156661$ K $^{-1}$ (based on Lide (1995) data cover-
 352 ing $T=160-300$ K). Re-evaporation of any condensate below the tropopause
 353 cold trap was suppressed to avoid unphysically high abundances in the
 354 troposphere.
- 355 • **Photochemical profile:** Where we used the photochemical profile
 356 of Lavvas et al. (2008). This profile was simply scaled to vary the
 357 abundance, but the VMR in the lower stratosphere was limited by the
 358 saturation vapour pressure equation above.

359 These profiles are shown in Figure 6.

360 5. Results

361 Figure 7 shows χ^2 as a function of NH_3 abundance for uniform and pho-
 362 tochemical profile cases. Neither case has a minimum χ^2 below $\chi^2(0) - 18$,
 363 implying that we do not detect NH_3 at the 3-sigma level with these data.
 364 Instead our data gives 3-sigma upper limits (corresponding to $\chi^2(0) + 18$)

365 with a VMR of <0.19 ppb for the uniform profile and a scale factor of <53
 366 for the scaled photochemical profile of Lavvas et al. (2008). The contribu-
 367 tion functions at these kind of abundances peak at 75 km (FWHM between
 368 65–110 km), so sound the lower stratosphere. Synthetic spectra, created as-
 369 suming these upper limits, are shown in Figure 8 for the spectral regions
 370 surrounding the two strongest NH_3 features. In addition to having no formal
 371 statistically significant abundance, a visual inspection of the spectra shows
 372 no observable NH_3 emission features above the noise.

373 **6. Discussion and Conclusions**

374 The SPIRE data considered here give 3-sigma upper limits on Titan’s
 375 stratospheric NH_3 of 0.19 ppb assuming a uniform profile, or 53 times the
 376 Lavvas et al. (2008) photochemical profile. These constraints are an order
 377 of magnitude better than the previous best upper limit of 1.3 ppb from
 378 Cassini CIRS (Nixon et al., 2010). This improvement is mainly a result of
 379 the factor of 10 improvement in spectral resolution obtained with SPIRE,
 380 while maintaining comparable noise levels to CIRS. Our values correspond
 381 to total column abundances of $<1.23 \times 10^{15}$ molecules/cm² (uniform) and
 382 $<0.94 \times 10^{15}$ molecules/cm² (photochemical), which is a relatively profile-
 383 independent measure. Therefore, the only current detection of NH_3 in Titan’s
 384 atmosphere remains the in-situ measurement of 7×10^{-6} at 1100km by Cassini
 385 INMS (Vuitton et al., 2007; Vuitton et al., 2009). If the Lavvas et al. (2008)
 386 profile is scaled by a factor of 33.5 to match the INMS value (as done by
 387 Lellouch et al. (2010)), the resulting profile falls just below our upper limit
 388 so is still consistent with the SPIRE data.

389 Figure 9a compares our results to available predicted NH_3 profiles from
390 the literature (Wilson and Atreya, 2004; Krasnopolsky, 2009; Lavvas et al.,
391 2008). While our new results provide a much improved constraint in the
392 lower stratosphere, the only profile that can actually be ruled out based on
393 our data is the supplemental case in Krasnopolsky (2009) which used the
394 modified Hörst values (Hörst et al., 2008) for the eddy mixing profile. All
395 other profiles fall below our upper limit at 75 km altitude.

396 If volume mixing ratio profiles are scaled in order to fit the INMS obser-
397 vation at 1100 km (Figure 9b), then both Krasnopolsky (2009) profiles can
398 be ruled out. However, the application of such a simple scaling is a gross
399 oversimplification of the effect of increased NH_3 abundance at 1100 km and
400 does not provide a rigorous test of the models. Therefore, the abundance of
401 NH_3 in Titan’s stratosphere remains an open question. Prospects for future
402 detection of NH_3 in the sub-millimetre range remain promising, but will re-
403 quire an improvement in sensitivity of an order of magnitude or more before
404 photochemical predictions can be tested further. Therefore, while our upper
405 limit is the most stringent to date, we must await future missions to improve
406 the accuracy and draw more insightful conclusions about Titan’s ammonia
407 cycle.

408 7. Acknowledgements

409 This work was funded by the UK Science and Technology Facilities Coun-
410 cil and the Leverhulme Trust. SPIRE has been developed by a consortium
411 of institutes led by Cardiff University (UK) and including Univ. Lethbridge
412 (Canada); NAOC (China); CEA, LAM (France); IFSI, Univ. Padua (Italy);

413 IAC (Spain); Stockholm Observatory (Sweden); Imperial College London,
414 RAL, UCL-MSSL, UKATC, Univ. Sussex (UK); and Caltech, JPL, NHSC,
415 Univ. Colorado (USA). This development has been supported by national
416 funding agencies: CSA (Canada); NAOJ (China); CEA, CNES, CNRS
417 (France); ASI (Italy); MCINN (Spain); SNSB (Sweden); STFC (UK); and
418 NASA (USA).

419 **References**

- 420 Anderson, C.M., Samuelson, R.E., 2011. Titan’s aerosol and stratospheric
421 ice opacities between 18 and 500 μm : Vertical and spectral characteristics
422 from Cassini CIRS. *Icarus* 212, 762–778.
- 423 Borysow, A., 1991. Modelling of collision-induced infrared-absorption spectra
424 of $\text{H}_2\text{-H}_2$ pairs in the fundamental band at temperatures from 20K to 300K.
425 *Icarus* 92, 273–279.
- 426 Borysow, A., Frommhold, L., 1986a. Collision-induced rototranslational ab-
427 sorption spectra of $\text{N}_2\text{-N}_2$ pairs for temperatures from 50 to 300K. *Astro-*
428 *phys. J.* 311, 1043–1057.
- 429 Borysow, A., Frommhold, L., 1986b. Theoretical collision-induced rototrans-
430 lational absorption spectra for modeling Titan’s atmosphere: $\text{H}_2\text{-N}_2$ pairs.
431 *Astrophys. J.* 303, 495–510.
- 432 Borysow, A., Frommhold, L., 1986c. Theoretical collision-induced rototrans-
433 lational absorption spectra for the outer planets: $\text{H}_2\text{-CH}_4$ pairs. *Astrophys.*
434 *J.* 304, 849–865.

435 Borysow, A., Frommhold, L., 1987. Collision-induced rototranslational ab-
436 sorption spectra of CH₄-CH₄ pairs at temperatures from 50 to 300K. As-
437 trophys. J. 318, 940–943.

438 Borysow, A., Tang, C., 1993. Far infrared CIA spectra of N₂-CH₄ pairs for
439 modeling of Titan’s atmosphere. Icarus 105, 175–183.

440 Cottini, V., Nixon, C.A., Jennings, D.E., Anderson, C.M., Gorius, N., Bjo-
441 raker, G.L., Coustenis, A., Teanby, N.A., Achterberg, R.K., Bézard, B.,
442 de Kok, R., Lellouch, E., Irwin, P.G.J., Flasar, F.M., Bampasidis, G.,
443 2012. Water vapor in Titan’s stratosphere from Cassini CIRS far-infrared
444 spectra. Icarus 220, 855–862.

445 Courtin, R., Swinyard, B.M., Moreno, R., Fulton, T., Lellouch, E., Rengel,
446 M., Hartogh, P., 2011. First results of Herschel-SPIRE observations of
447 Titan. Astron. Astrophys. 536, L2.

448 Coustenis, A., Achterberg, R.K., Conrath, B.J., Jennings, D.E., Marten,
449 A., Gautier, D., Nixon, C.A., Flasar, F.M., Teanby, N.A., Bézard, B.,
450 Samuelson, R.E., Carlson, R.C., Lellouch, E., Bjoraker, G.L., Romani,
451 P.N., Taylor, F.W., Irwin, P.G., Fouchet, T., Hubert, A., Orton, G.S.,
452 Kunde, V.G., Vinatier, S., Mondellini, J., Abbas, M.M., Courtin, R., 2007.
453 The composition of Titan’s stratosphere from Cassini/CIRS mid-infrared
454 spectra. Icarus 189, 35–62.

455 Coustenis, A., Nixon, C., Achterberg, R., Lavvas, P., Vinatier, S., Teanby, N.,
456 Bjoraker, G., Carlson, R., Piani, L., Bampasidis, G., Flasar, F., Romani,

457 P., 2010. Titan trace gaseous composition from CIRS at the end of the
 458 Cassini-Huygens prime mission. *Icarus* 207, 461–476.

459 Fischer, J., Gamache, R.R., Goldman, A., Rothman, L.S., Perrin, A., 2003.
 460 Total internal partition sums for molecular species in the 2000 edition of
 461 the HITRAN database. *J. Quant. Spectro. Rad. Trans.* 82, 401–412.

462 Flasar, F.M., Achterberg, R.K., Conrath, B.J., Gierasch, P.J., Kunde, V.G.,
 463 Nixon, C.A., Bjoraker, G.L., Jennings, D.E., Romani, P.N., Simon-Miller,
 464 A.A., Bézard, B., Coustenis, A., Irwin, P.G.J., Teanby, N.A., Brasunas,
 465 J., Pearl, J.C., Segura, M.E., Carlson, R.C., Mamoutkine, A., Schinder,
 466 P.J., Barucci, A., Courtin, R., Fouchet, T., Gautier, D., Lellouch, E.,
 467 Marten, A., Prange, R., Vinatier, S., Strobel, D.F., Calcutt, S.B., Read,
 468 P.L., Taylor, F.W., Bowles, N., Samuelson, R.E., Orton, G.S., Spilker,
 469 L.J., Owen, T.C., Spencer, J.R., Showalter, M.R., Ferrari, C., Abbas,
 470 M.M., Raulin, F., Edgington, S., Ade, P., Wishnow, E.H., 2005. Titan’s
 471 atmospheric temperatures, winds, and composition. *Science* 308, 975–978.

472 Flasar, F.M., Kunde, V.G., Abbas, M.M., Achterberg, R.K., Ade, P.,
 473 Barucci, A., Bézard, B., Bjoraker, G.L., Brasunas, J.C., Calcutt, S.,
 474 Carlson, R., Esarsky, C.J.C., Conrath, B.J., Coradini, A., Courtin, R.,
 475 Coustenis, A., Edberg, S., Edgington, S., Ferrari, C., Fouchet, T., Gau-
 476 tier, D., Gierasch, P.J., Grossman, K., Irwin, P., Jennings, D.E., Lel-
 477 louch, E., Mamoutkine, A.A., Marten, A., Meyer, J.P., Nixon, C.A., Or-
 478 ton, G.S., Owen, T.C., Pearl, J.C., Prange, R., Raulin, F., Read, P.L.,
 479 Romani, P.N., Samuelson, R.E., Segura, M.E., Showalter, M.R., Simon-
 480 Miller, A.A., Smith, M.D., Spencer, J.R., Spilker, L.J., Taylor, F.W., 2004.

481 Exploring the Saturn system in the thermal infrared: The Composite In-
482 frared Spectrometer. *Space Sci. Rev.* 115, 169–297.

483 Forbes, C., Evans, M., Hastings, N., Peacock, B., 2011. *Statistical Distribu-*
484 *tions*. Wiley, Hoboken, New Jersey. 4th edition.

485 Fulchignoni, M., Ferri, F., Angrilli, F., Ball, A.J., Bar-Nun, A., Barucci,
486 M.A., Bettanini, C., Bianchini, G., Borucki, W., Colombatti, G., Coradini,
487 M., Coustenis, A., Debei, S., Falkner, P., Fanti, G., Flamini, E., Gaborit,
488 V., Grard, R., Hamelin, M., Harri, A.M., Hathi, B., Jernej, I., Leese, M.R.,
489 Lehto, A., Stoppato, P.F.L., Lopez-Moreno, J.J., Makinen, T., McDonnell,
490 J.A.M., McKay, C.P., Molina-Cuberos, G., Neubauer, F.M., Pirronello, V.,
491 Rodrigo, R., Saggin, B., Schwingenschuh, K., Seiff, A., Simoes, F., Sved-
492 hem, H., Tokano, T., Towner, M.C., Trautner, R., Withers, P., Zarnecki,
493 J.C., 2005. In situ measurements of the physical characteristics of Titan’s
494 environment. *Nature* 438, 785–791.

495 Hartogh, P., Lellouch, E., Crovisier, J., Banaszkiewicz, M., Bensch, F.,
496 Bergin, E.A., Billebaud, F., Biver, N., Blake, G.A., Blecka, M.I., Blom-
497 maert, J., Bockelée-Morvan, D., Cavalié, T., Cernicharo, J., Courtin, R.,
498 Davis, G., Decin, L., Encrenaz, P., Encrenaz, T., González, A., de Graauw,
499 T., Hutsemékers, D., Jarchow, C., Jehin, E., Kidger, M., Küppers, M., de
500 Lange, A., Lara, L.M., Lis, D.C., Lorente, R., Manfroid, J., Medvedev,
501 A.S., Moreno, R., Naylor, D.A., Orton, G., Portyankina, G., Rengel, M.,
502 Sagawa, H., Sánchez-Portal, M., Schieder, R., Sidher, S., Stam, D., Swin-
503 yard, B., Szutowicz, S., Thomas, N., Thornhill, G., Vandenbussche, B.,
504 Verdugo, E., Waelkens, C., Walker, H., 2009. *Water and related chemistry*

505 in the solar system. A guaranteed time key programme for Herschel. *Plan.*
506 & *Space Sci.* 57, 1596–1606.

507 Hörst, S.M., Vuitton, V., Yelle, R.V., 2008. Origin of oxygen species in
508 Titan’s atmosphere. *J. Geophys. Res.* 113, E10006.

509 Irwin, P., Teanby, N., de Kok, R., Fletcher, L., Howett, C., Tsang, C., Wil-
510 son, C., Calcutt, S., Nixon, C., Parrish, P., 2008. The NEMESIS planetary
511 atmosphere radiative transfer and retrieval tool. *J. Quant. Spectro. Rad.*
512 *Trans.* 109, 1136–1150.

513 de Kok, R., Irwin, P.G.J., Teanby, N.A., Lellouch, E., Bezard, B., Vinatier,
514 S., Nixon, C.A., Fletcher, L., Howett, C., Calcutt, S.B., Bowles, N.E.,
515 Flasar, F.M., Taylor, F.W., 2007a. Oxygen compounds in Titan’s strato-
516 sphere as observed by Cassini CIRS. *Icarus* 186, 354–363.

517 de Kok, R., Irwin, P.G.J., Teanby, N.A., Nixon, C.A., Jennings, D.E.,
518 Fletcher, L., Howett, C., Calcutt, S.B., Bowles, N.E., Flasar, F.M., Taylor,
519 F.W., 2007b. Characteristics of Titan’s stratospheric aerosols and conden-
520 sate clouds from Cassini CIRS far-infrared spectra. *Icarus* 191, 223–235.

521 de Kok, R., Irwin, P.G.J., Teanby, N.A., Vinatier, S., Negrão, A., Osprey, S.,
522 Adriani, A., Moriconi, M.L., A., C., 2010. A tropical haze band in Titan’s
523 stratosphere. *Icarus* 207, 485–490.

524 Krasnopolsky, V.A., 2009. A photochemical model of titan’s atmosphere and
525 ionosphere. *Icarus* 201, 226–256.

526 Lacis, A.A., Oinas, V., 1991. A description of the correlated k distribution
527 method for modeling nongray gaseous absorption, thermal emission, and

multiple-scattering in vertically inhomogeneous atmospheres. *J. Geophys. Res.* 96, 9027–9063.

Lavvas, P.P., Coustenis, A., Vardavas, I.M., 2008. Coupling photochemistry with haze formation in Titan’s atmosphere, Part II: Results and validation with Cassini/Huygens data. *Plan. & Space Sci.* 56, 67–99.

Lellouch, E., Vinatier, S., Moreno, R., Allen, M., Gulkis, S., Hartogh, P., Krieg, J.M., Maestrini, A., Mehdi, I., Coustenis, A., 2010. Sounding of Titan’s atmosphere at submillimeter wavelengths from an orbiting spacecraft. *Plan. & Space Sci.* 58, 1724–1739.

Lide, D.R. (Ed.), 1995. *CRC handbook of chemistry and physics*. CRC Press, Inc., Boca Raton. 76th edition.

Moreno, R., Lellouch, E., Lara, L.M., Courtin, R., Bockelée-Morvan, D., Hartogh, P., Rengel, M., Biver, N., Banaszkiewicz, M., González, A., 2011. First detection of hydrogen isocyanide (HNC) in Titan’s atmosphere. *Astron. Astrophys.* 536, L12.

Moreno, R., Lellouch, E., Lara, L.M., Feuchtgruber, H., Rengel, M., Hartogh, P., Courtin, R., 2012. The abundance, vertical distribution and origin of H₂O in Titan’s atmosphere: Herschel observations and photochemical modelling. *Icarus* in press, doi:10.1016/j.icarus.2012.09.006.

Niemann, H.B., Atreya, S.K., Demick, J.E., Gautier, D., Haberman, J.A., Harpold, D.N., Kasprzak, W.T., Lunine, J.I., Owen, T.C., Raulin, F., 2010. Composition of Titan’s lower atmosphere and simple surface volatiles

550 as measured by the Cassini-Huygens probe gas chromatograph mass spec-
 551 trometer experiment. *J. Geophys. Res.* 115, E12006.

552 Nixon, C.A., Achterberg, R.K., Teanby, N.A., Irwin, P.G.J., Flaud, J.M.,
 553 Kleiner, I., Dehayem-Kamadjeu, A., Brown, L.R., Sams, R.L., Bézard,
 554 B., Coustenis, A., Ansty, T.M., Mamoutkine, A., Vinatier, S., Bjoraker,
 555 G.L., Jennings, D.E., Romani, P.N., Flasar, F.M., 2010. Upper limits for
 556 undetected trace species in the stratosphere of Titan. *Faraday Discussions*
 557 147, 65–81.

558 Nixon, C.A., Jennings, D.E., Flaud, J.M., Bezard, B., Teanby, N.A., Irwin,
 559 P.G.J., Ansty, T.M., Coustenis, A., Vinatier, S., Flasar, F.M., 2009. Ti-
 560 tan’s prolific propane: The Cassini CIRS perspective. *Plan. & Space Sci.*
 561 57, 1573–1585.

562 Pilbratt, G.L., Riedinger, J.R., Passvogel, T., Crone, G., Doyle, D., Gageur,
 563 U., Heras, A.M., Jewell, C., Metcalfe, L., Ott, S., Schmidt, M., 2010. Her-
 564 schel Space Observatory. An ESA facility for far-infrared and submillimetre
 565 astronomy. *Astron. Astrophys.* 518, L1.

566 Press, W.H., Flannery, B.P., Teukolsky, S.A., Vetterling, W.T., 1992. Nu-
 567 merical Recipes. Cambridge Univ. Press, Cambridge UK. 2nd edition.

568 Rothman, L.S., Jacquemart, D., Barbe, A., Benner, D.C., Birk, M., Brown,
 569 L.R., Carleer, M.R., Chackerian, C., Chance, K., Coudert, L.H., Dana, V.,
 570 Devi, V.M., Flaud, J.M., Gamache, R.R., Goldman, A., Hartmann, J.M.,
 571 Jucks, K.W., Maki, A.G., Mandin, J.Y., Massie, S.T., Orphal, J., Perrin,
 572 A., Rinsland, C.P., Smith, M.A.H., Tennyson, J., Tolchenov, R.N., Toth,

573 R.A., Vander Auwera, J., Varanasi, P., Wagner, G., 2005. The HITRAN
574 2004 molecular spectroscopic database. *J. Quant. Spectro. Rad. Trans.* 96,
575 139–204.

576 Swinyard, B.M., Ade, P., Baluteau, J.P., Aussel, H., Barlow, M.J., Bendo,
577 G.J., Benielli, D., Bock, J., Brisbin, D., Conley, A., Conversi, L., Dowell,
578 A., Dowell, D., Ferlet, M., Fulton, T., Glenn, J., Glauser, A., Griffin, D.,
579 Griffin, M., Guest, S., Imhof, P., Isaak, K., Jones, S., King, K., Leeks,
580 S., Levenson, L., Lim, T.L., Lu, N., Makiwa, G., Naylor, D., Nguyen,
581 H., Oliver, S., Panuzzo, P., Papageorgiou, A., Pearson, C., Pohlen, M.,
582 Polehampton, E., Pouliquen, D., Rigopoulou, D., Ronayette, S., Roussel,
583 H., Rykala, A., Savini, G., Schulz, B., Schwartz, A., Shupe, D., Sibthorpe,
584 B., Sidher, S., Smith, A.J., Spencer, L., Trichas, M., Triou, H., Valtchanov,
585 I., Wesson, R., Woodcraft, A., Xu, C.K., Zemcov, M., Zhang, L., 2010. In-
586 flight calibration of the Herschel-SPIRE instrument. *Astron. Astrophys.*
587 518, L4.

588 Teanby, N.A., 2007. Constrained smoothing of noisy data using splines in
589 tension. *Math. Geol.* 39, 419–434.

590 Teanby, N.A., Fletcher, L.N., Irwin, P.G.J., Fouchet, T., Orton, G.S., 2006a.
591 New upper limits for hydrogen halides on Saturn derived from Cassini-
592 CIRS data. *Icarus* 185, 466–475.

593 Teanby, N.A., Irwin, P.G.J., 2007. Quantifying the effect of finite field-of-view
594 size on radiative transfer calculations of Titan’s limb spectra measured by
595 Cassini-CIRS. *Astrophys. & Space Sci.* 310, 293–305.

- 596 Teanby, N.A., Irwin, P.G.J., de Kok, R., Jolly, A., Bézard, B., Nixon, C.A.,
597 Calcutt, S.B., 2009a. Titan’s stratospheric C_2N_2 , C_3H_4 , and C_4H_2 abun-
598 dances from Cassini/CIRS far-infrared spectra. *Icarus* 202, 620–631.
- 599 Teanby, N.A., Irwin, P.G.J., de Kok, R., Nixon, C.A., 2009b. Dynami-
600 cal implications of seasonal and spatial variations in Titan’s stratospheric
601 composition. *Phil. Trans. R. Soc. Lond. A* 367, 697–711.
- 602 Teanby, N.A., Irwin, P.G.J., de Kok, R., Nixon, C.A., Coustenis, A., Royer,
603 E., Calcutt, S.B., Bowles, N.E., Fletcher, L., Howett, C., Taylor, F.W.,
604 2008a. Global and temporal variations in hydrocarbons and nitriles in
605 Titan’s stratosphere for northern winter observed by Cassini/CIRS. *Icarus*
606 193, 595–611.
- 607 Teanby, N.A., Irwin, P.G.J., de Kok, R., 2010a. Compositional evidence for
608 Titan’s stratospheric tilt. *Plan. & Space Sci.* 58, 792–800.
- 609 Teanby, N.A., Irwin, P.G.J., de Kok, R., Nixon, C.A., 2010b. Mapping
610 Titan’s HCN in the far infra-red: implications for photochemistry. *Faraday*
611 *Discussions* 147, 51–64.
- 612 Teanby, N.A., Irwin, P.G.J., de Kok, R., Nixon, C.A., 2010c. Seasonal
613 changes in Titan’s polar trace gas abundance observed by Cassini. *As-*
614 *trophys. J.* 724, L84–L89.
- 615 Teanby, N.A., Irwin, P.G.J., de Kok, R., Nixon, C.A., Coustenis, A., Bézard,
616 B., Calcutt, S.B., Bowles, N.E., Flasar, F.M., Fletcher, L., Howett, C.,
617 Taylor, F.W., 2006b. Latitudinal variations of HCN, HC_3N , and C_2N_2 in
618 Titan’s stratosphere derived from Cassini CIRS data. *Icarus* 181, 243–255.

- 619 Teanby, N.A., Irwin, P.G.J., de Kok, R., Vinatier, S., Bézard, B., Nixon,
620 C.A., Flasar, F.M., Calcutt, S.B., Bowles, N.E., Fletcher, L., Howett, C.,
621 Taylor, F.W., 2007. Vertical profiles of HCN, HC₃N, and C₂H₂ in Titan's
622 atmosphere derived from Cassini/CIRS data. *Icarus* 186, 364–384.
- 623 Teanby, N.A., de Kok, R., Irwin, P.G.J., Osprey, S., Vinatier, S., Gierasch,
624 P.J., Read, P.L., Flasar, F.M., Conrath, B.J., Achterberg, R.K., Bézard,
625 B., Nixon, C.A., Calcutt, S.B., 2008b. Titan's winter polar vortex structure
626 revealed by chemical tracers. *J. Geophys. Res.* 113, E12003.
- 627 Tomasko, M.G., Doose, L., Engel, S., Dafoe, L.E., West, R., Lemmon, M.,
628 Karkoschka, E., See, C., 2008. A model of Titan's aerosols based on mea-
629 surements made inside the atmosphere. *Plan. & Space Sci.* 56, 669–707.
- 630 Vinatier, S., Bézard, B., Fouchet, T., Teanby, N.A., de Kok, R., Irwin, P.G.J.,
631 Conrath, B.J., Nixon, C.A., Romani, P.N., Flasar, F.M., Coustenis, A.,
632 2007. Vertical abundance profiles of hydrocarbons in Titan's atmosphere
633 at 15°S and 80°N retrieved from Cassini/CIRS spectra. *Icarus* 188, 120–
634 138.
- 635 Vinatier, S., Bézard, B., Nixon, C.A., Mamoutkine, A., Carlson, R.C., Jen-
636 nings, D.E., Guandique, E.A., Teanby, N.A., Bjoraker, G.L., Flasar, F.M.,
637 Kunde, V.G., 2010. Analysis of Cassini/CIRS limb spectra of Titan ac-
638 quired during the nominal mission I. hydrocarbons, nitriles and CO₂ ver-
639 tical mixing ratio profiles. *Icarus* 205, 559–570.
- 640 Vuitton, V., Yelle, R.V., Lavvas, P., 2009. Composition and chemistry of

- 641 Titan's thermosphere and ionosphere. *Phil. Trans. R. Soc. Lond. A* 367,
642 729–741.
- 643 Vuitton, V., Yelle, R.V., McEwan, M.J., 2007. Ion chemistry and N-
644 containing molecules in Titan's upper atmosphere. *Icarus* 191, 722–742.
- 645 Waite, J.H., Niemann, H., Yelle, R.V., Kasprzak, W.T., Cravens, T.E., Luh-
646 mann, J.G., McNutt, R.L., Ip, W.H., Gell, D., De La Haye, V., Muller-
647 Wordag, I., Magee, B., Borggren, N., Ledvina, S., Fletcher, G., Walter,
648 E., Miller, R., Scherer, S., Thorpe, R., Xu, J., Block, B., Arnett, K., 2005.
649 Ion neutral mass spectrometer results from the first flyby of Titan. *Science*
650 308, 982–986.
- 651 Wilson, E.H., Atreya, S.K., 2004. Current state of modeling the photo-
652 chemistry of Titan's mutually dependent atmosphere and ionosphere. *J.*
653 *Geophys. Res.* 109, E06002.
- 654 Wilson, T.L., Rohlfs, K., Hüttemeister, S., 2009. *Tools of Radio Astronomy*.
655 Springer-Verlag, Berlin. 5th edition.
- 656 Wishnow, E.H., Orton, G.S., Ozier, I., Gush, H.P., 2007. The distortion
657 dipole rotational spectrum of CH₄: A low temperature far-infrared study.
658 *J. Quant. Spectro. Rad. Trans.* 103, 102–117.
- 659 Yelle, R.V., Vuitton, V., Lavvas, P., Klippenstein, S.J., Smith, M.A., Hörst,
660 S.M., Cui, J., 2010. Formation of NH₃ and CH₂NH in Titan's upper
661 atmosphere. *Faraday Discussions* 147, 31–49.

Obs.	Product ID	Start Time	Integration Time	Sub-Herschel Point		Shift
		(UT)	(s)	Longitude ($^{\circ}$ W)	Latitude ($^{\circ}$ N)	(cm^{-1})
S0†	1342198925	2010-06-22 12:11:54	1322	273.58	2.05	-
S1	1342201495	2010-07-16 03:44:14	31878	89.43	2.73	+0.0013
S2	1342224755	2011-07-25 23:38:55	10786	235.65	8.09	+0.0042
S3	1342224756	2011-07-26 02:38:55	10786	260.99	8.13	+0.0041
S4	1342224757	2011-07-26 05:38:55	10786	263.80	8.13	+0.0045

Table 1: Details of the SSW observations used in this paper. Sub-Herschel point is given for observation mid-point. Shift is wavenumber correction applied to observation to give the best match to the reference spectrum. All spectra cover a wavelength range of $31.2\text{--}51.8\text{ cm}^{-1}$ with an unapodised / apodised spectral resolution of $0.048 / 0.07373\text{ cm}^{-1}$. †Observation on 22/6/2010 was not used due to contamination from Saturn and low signal-to-noise.

Wavenumber	Cross section	τ
(cm^{-1})	($\text{cm}^2/\text{particle}$)	
30	1.30×10^{-10}	1.6×10^{-9}
35	6.18×10^{-05}	7.5×10^{-4}
40	1.59×10^{-04}	1.9×10^{-3}
45	2.65×10^{-04}	3.2×10^{-3}
50	4.61×10^{-04}	5.6×10^{-3}
55	6.13×10^{-04}	7.5×10^{-3}
[160	1.26×10^{-03}	$1.5 \times 10^{-2}]$

Table 2: Relative absorption cross sections assumed for Titan’s main haze as a function of wavenumber. τ is the integrated nadir column optical depth using the specific particle density profile in Figure 6. The low optical depths show that haze has a very minor effect on Titan’s spectrum at these wavelengths. While not covered by the SPIRE FTS, values at 160 cm^{-1} are also given to allow comparison with Anderson and Samuelson (2011).

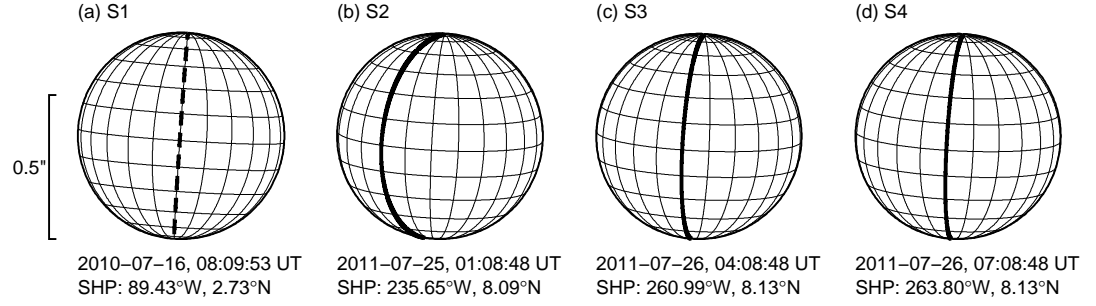


Figure 1: Viewing geometry of Titan for the four observations analysed in this paper. Date and time are for observation mid-point. SHP is the longitude and latitude of the sub-Herschel point. Solid bold line indicates the 270°W meridian and bold dashed line indicates the 90°W meridian (0°W is the sub-Saturn direction).

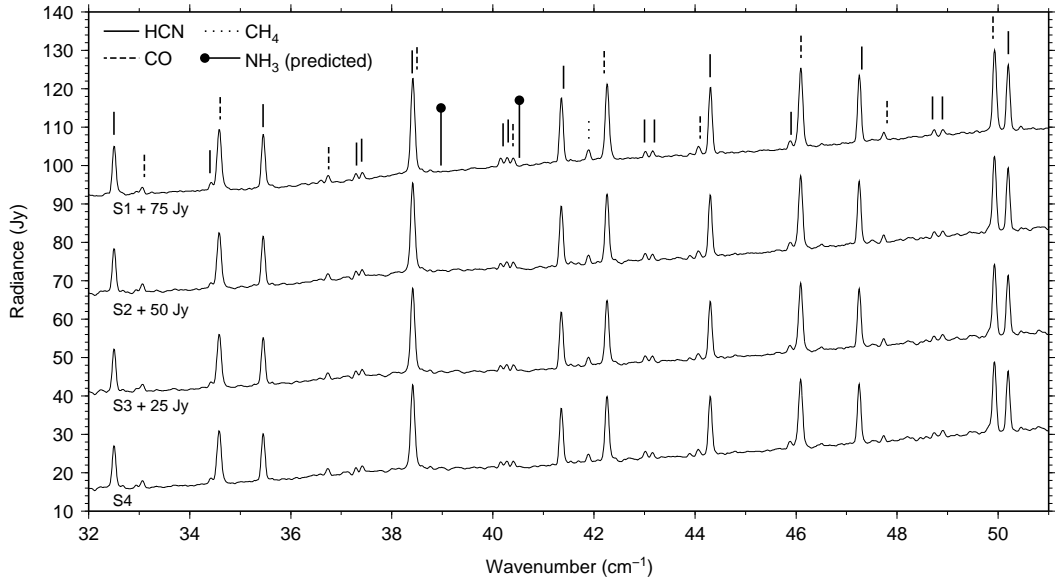


Figure 2: Level 2 processed SSW spectra after convolution with a Hamming apodisation function with a FWHM of 0.07373 cm^{-1} for the four SPIRE observations. Spectra are offset vertically for clarity as indicated. The positions of emission features from CO, HCN, and CH₄ are indicated with vertical ticks. The predicted position of NH₃ lines are indicated by vertical ticks with blobs on. Note all visible emission peaks are accounted for by previously detected species.

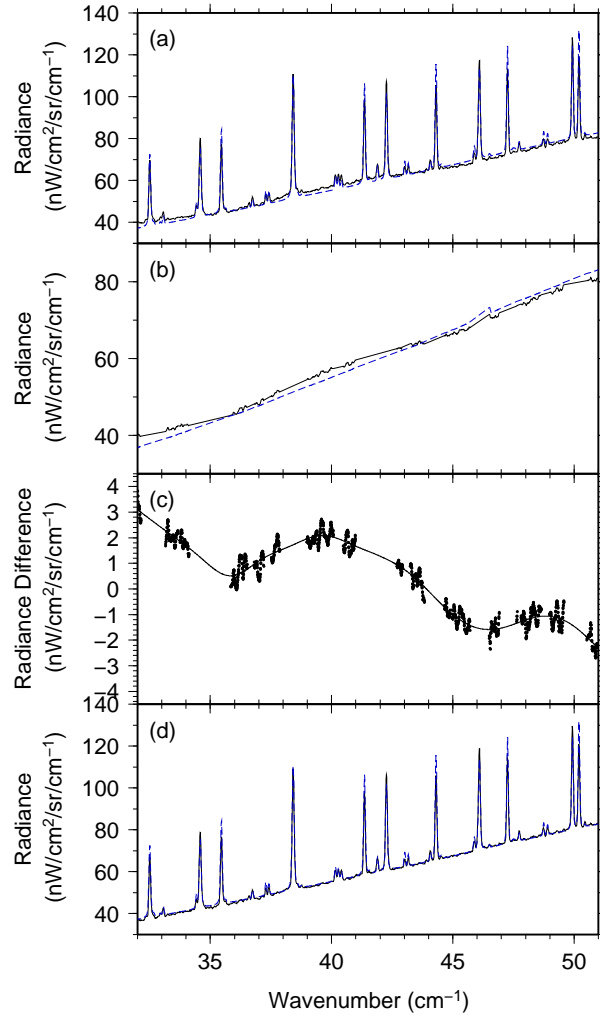


Figure 3: Illustration of baseline ripple removal procedure for observation S1. (a) Observed spectrum (solid line), after conversion to spectral radiance, compared with the synthetic reference spectrum (dashed blue line) generated based on Cassini constraints. Overall agreement is excellent considering no fitting has been attempted at this stage. (b) Observed continuum level (solid line) compared to reference spectrum (dashed blue line) after masking out gas emission peaks. (c) Residual between observation and reference spectrum (points) and best fitting spline curve (solid line). Small but significant continuum ripples due to instrument artifacts are evident. (d) Comparison of reference spectrum (dashed blue line) with ripple corrected observation (solid line). Such ripple corrected spectra form the basis of our analysis.

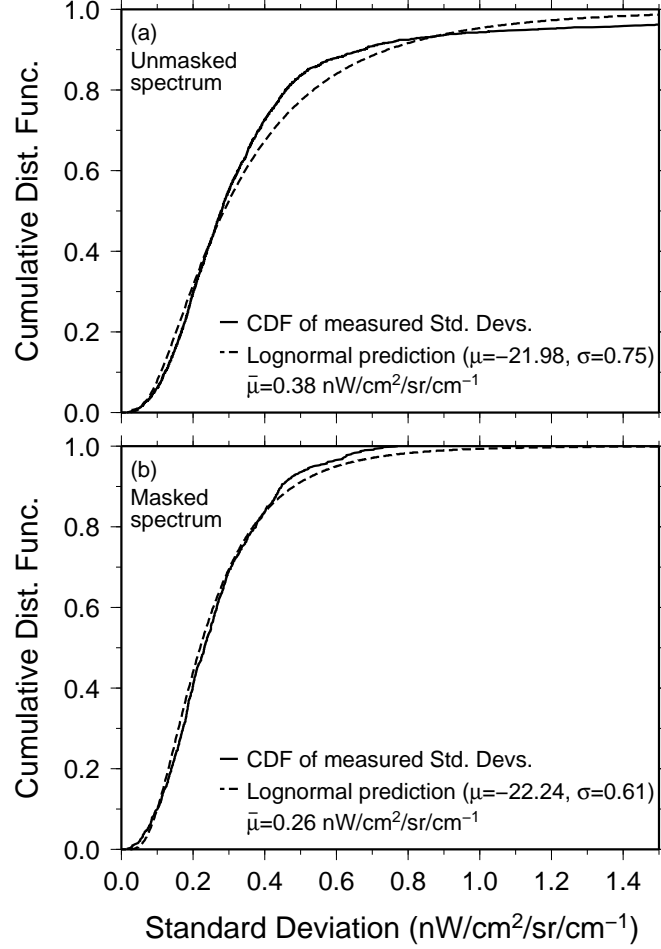


Figure 4: Cumulative distribution function of standard deviations $\delta(\nu_j)$ between the four SSW observations (solid line) compared to theoretical log-normal distribution with parameters $\mu=\text{mean}(\ln \delta)$ and $\sigma=\text{std. dev.}(\ln \delta)$. $\bar{\mu}$ is the equivalent mean value of the standard deviation corresponding to the plotted log-normal predicted CDF. (a) Distribution for all wavenumbers, indicating a tail of high standard deviations in the observed spectra. (b) Distribution of continuum-only wavenumbers, which matches the theoretical distribution very well - suggesting $\bar{\mu}$ is a representative standard deviation for our observations.

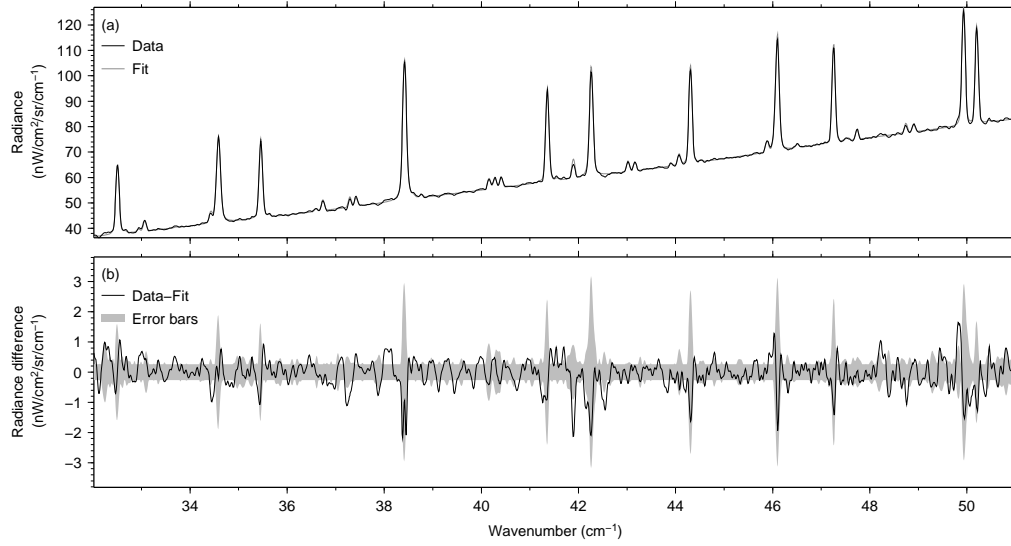


Figure 5: (a) Final average of four wavenumber and ripple corrected spectra. The fit and observation are indistinguishable on this plot. (b) Difference between average observed spectrum and fitted spectrum. Error bars $\overline{\sigma}(\nu_j)$ are shown with grey envelope and comprise the calculated standard deviation between the four observations $\delta(\nu_j)$, with a minimum value $\overline{\mu}$ set by the distribution fitted to the continuum standard deviation values in Figure 4. Note that increases in standard deviation are coincident with gas emission peaks and are caused by slight changes in geometry throughout the observation period combined with the non-spherically symmetric nature of Titan's atmosphere.

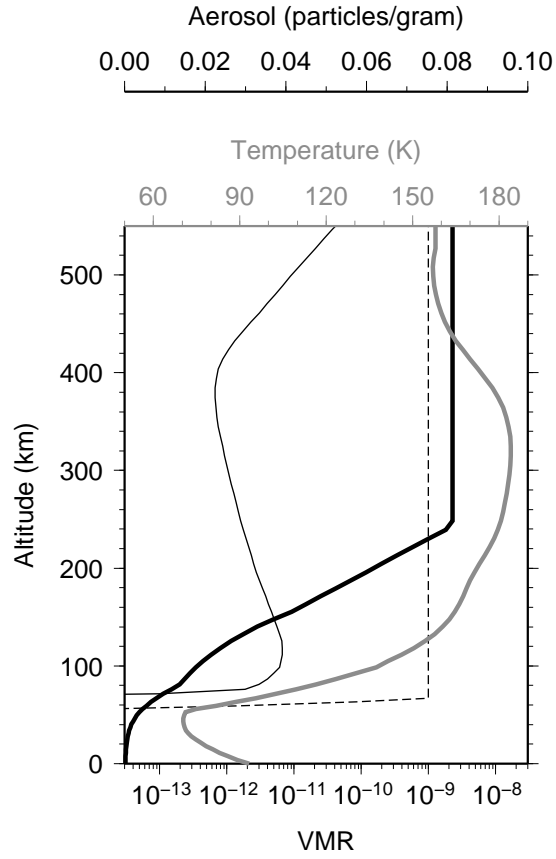


Figure 6: NH_3 profiles assumed during our analysis. Thin solid line is the Lavvas et al. (2008) photochemical NH_3 profile; thin dashed line is the uniform NH_3 profile, which condenses around 60 km altitude; the thick black line is the aerosol profile; and the thick grey solid line shows the temperature profile assumed throughout from Flasar et al. (2005).

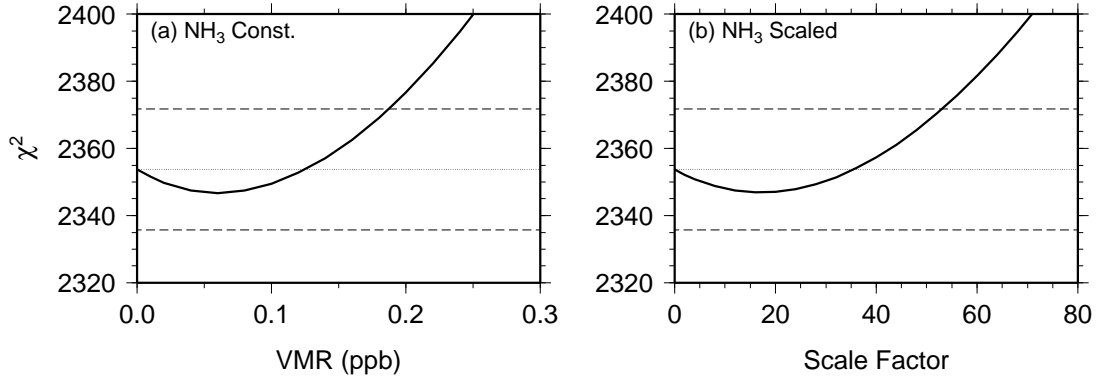


Figure 7: Variation of model-observation misfit $\chi^2(\alpha)$ as a function of NH_3 abundance α . (a) $\chi^2(\alpha)$ for a vertical volume mixing ratio profile that is constant above the condensation level. (b) $\chi^2(\alpha)$ obtained by scaling the photochemical profile of Lavvas et al. (2008). Lower dashed lines indicate 3-sigma detection criteria - that are not attained in either case. Upper dashed line gives the 3-sigma upper limit threshold. Upper limits are 0.19 ppb for the constant profile and a scale factor of 53 for the scaled Lavvas et al. (2008) profile.

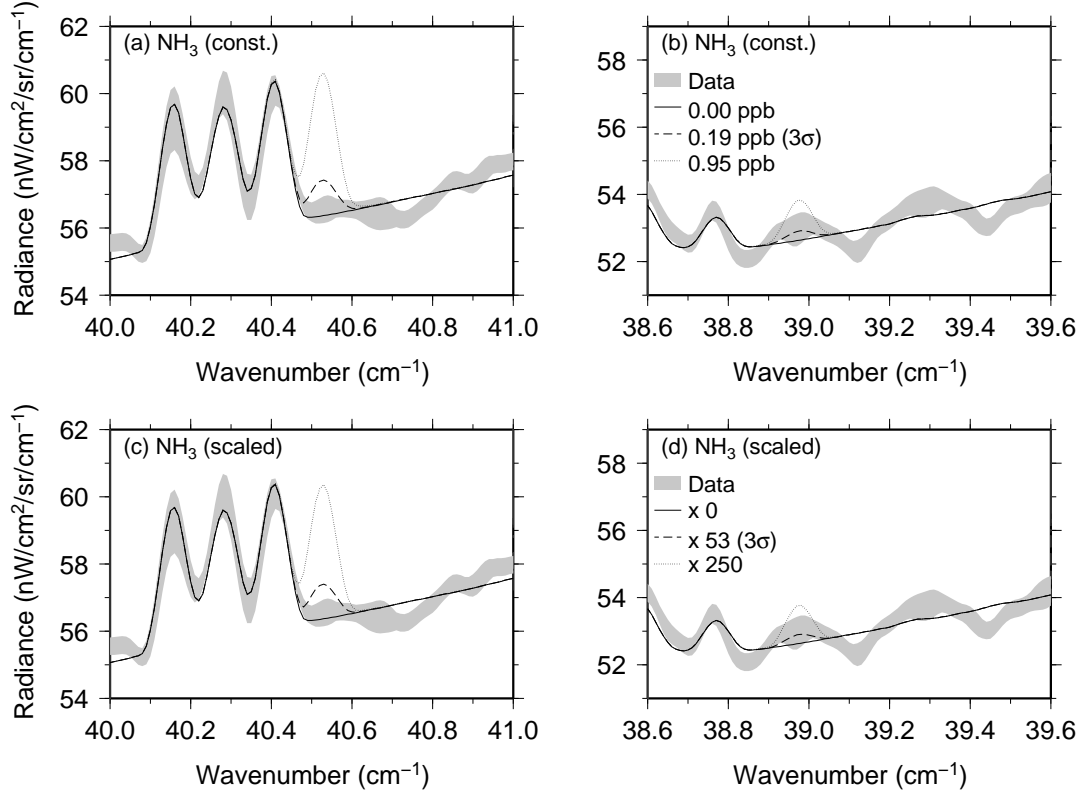


Figure 8: Close-up of spectral windows containing the two strongest NH_3 features in the SSW range. Data and error bars are indicated with grey envelope and lines show synthetic spectra with: no NH_3 (solid); NH_3 at the 3-sigma level (dashed); and five times the 3-sigma level to illustrate the NH_3 peak positions (dotted). (a,b) Show the constant VMR profile case and (c,d) show the scaled Lavvas et al. (2008) photochemical profile case. No spectral emission from NH_3 is visible in the data above the noise in either case. The three emission lines between 40.10 and 40.45 cm^{-1} correspond to HC^{15}N , C^{18}O , and ^{13}CO respectively.

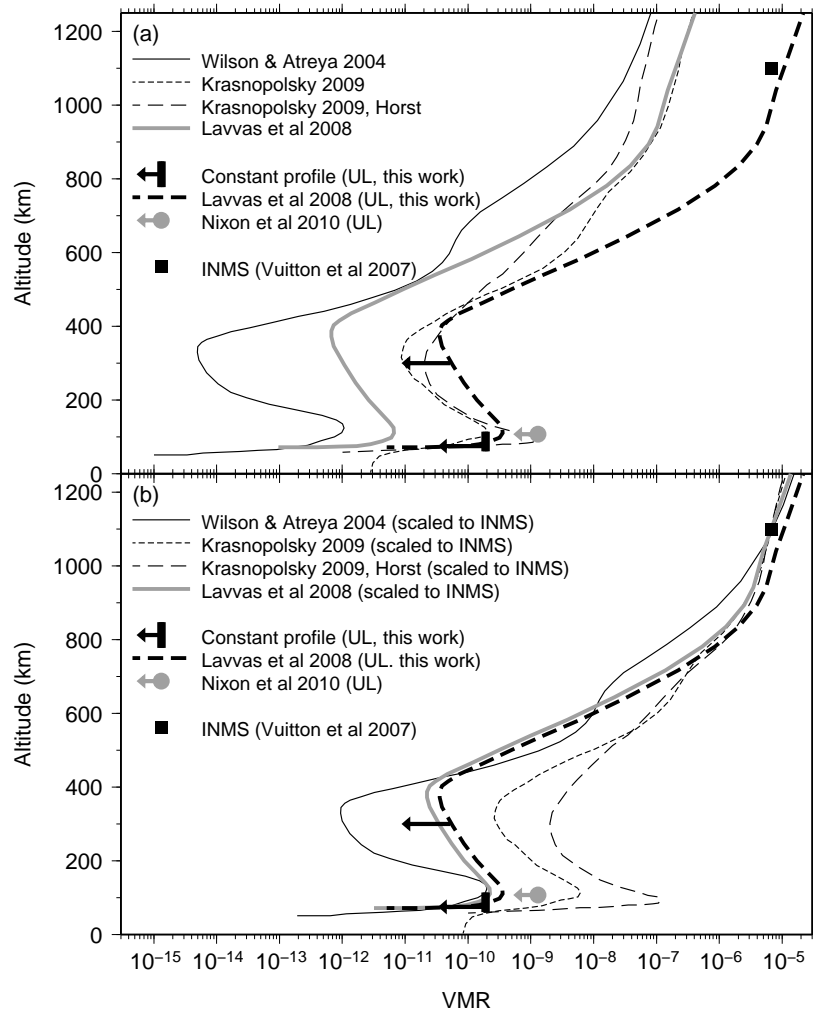


Figure 9: Comparison of our derived NH₃ upper limits with predicted photochemical profiles from the literature. The previous best upper limit (UL) from Nixon et al. (2010) is also shown for comparison. (a) Direct photochemical model output. All photochemical profiles are consistent with our upper limit, except Krasnopolsky’s case using the Hörst et al. (2008) eddy mixing profile (given in his appendix A). (b) Photochemical model output but rescaled to match the INMS measurement at 1100 km. In this case only the Lavvas et al. (2008) and Wilson and Atreya (2004) profiles are consistent with the data, although the assumption of linear scaling across 1000 km of atmosphere is unlikely to be representative of the full chemical complexity. Note that the secondary peaks at ≈ 100 km in the NH₃ photochemical model profiles are due to increased production related to cosmic rays.

662 Appendix A. Radiative transfer modelling of a disc-averaged spec- 663 trum

664 Figure A.10 shows the spectral radiance emitted by Titan as a function
665 of offset x from the sub-observer point, calculated using the reference atmo-
666 sphere from Section 3.2. There is significant emission beyond Titan’s solid
667 body radius of 2575 km due to its extended atmosphere. This manifests itself
668 as limb-brightening for both line and continuum emission.

669 Figure A.11 shows a synthetic Titan image based on the modelled radi-
670 ances in Figure A.10. The SSW field of view diameter D is much larger than
671 Titan’s diameter, resulting in a disc-averaged spectrum. Figures A.10 and
672 A.11 show that all emission from Titan can be considered to originate from
673 offsets of $x \leq r$, where $r=3000$ km. In section 3.1 we converted Janskys into
674 a disc-averaged spectral radiance \bar{s} assuming a circular emitting area with
675 radius r . This is defined by:

$$\bar{s} = \frac{\int_0^r \int_0^{2\pi} x s(x, \phi) d\phi dx}{\pi r^2} \quad (\text{A.1})$$

676 where $s(x, \phi)$ is the spectral radiance at offset x and azimuth ϕ on Titan’s
677 disc. Assuming a spherically symmetric planet gives rise to a radially sym-
678 metric radiance distribution across the disc, which results in the simplified
679 form:

$$\bar{s} = \frac{\int_0^r 2\pi x s(x) dx}{\pi r^2} \quad (\text{A.2})$$

680 In the forward model \bar{s} can be calculated as a weighted sum of P discrete
681 field-of-view averaging points (Teanby and Irwin, 2007) with offsets x_i and

682 calculated spectral radiances s_i . The problem is then to calculate the weights
 683 w_i to assign to each of these points, which we solve as follows.

684 The continuous form of Equation (A.2) for \bar{s} can be approximated in the
 685 case of discrete radiance points by:

$$\bar{s} \approx \frac{\sum_{i=1}^P \bar{s}_i \pi (x_{i+1}^2 - x_i^2)}{\pi r^2} \quad (\text{A.3})$$

686 where \bar{s}_i is area weighted mean spectral radiance for the annulus bounded
 687 by x_i and x_{i+1} (Figure A.11b):

$$\bar{s}_i = \frac{\int_{x_i}^{x_{i+1}} 2\pi x s(x) dx}{\pi (x_{i+1}^2 - x_i^2)} \quad (\text{A.4})$$

688 By assuming linear variation of $s(x)$ with offset x , the integral form can
 689 be replaced using the trapezium rule with:

$$\bar{s}_i = \frac{2\pi (x_{i+1} - x_i) (x_i s_i + x_{i+1} s_{i+1}) / 2}{\pi (x_{i+1}^2 - x_i^2)} \quad (\text{A.5})$$

$$= \frac{(x_i s_i + x_{i+1} s_{i+1})}{(x_i + x_{i+1})} \quad (\text{A.6})$$

690 The total disc-averaged spectral radiance is then given by substitution
 691 into Equation (A.3)

$$\bar{s} \approx \frac{\sum_{i=1}^P (x_i s_i + x_{i+1} s_{i+1}) (x_{i+1} - x_i)}{r^2} \quad (\text{A.7})$$

692 This expression can be expanded to give the FOV weights w_i for each
 693 discrete spectral radiance s_i :

$$w_1 = \frac{x_1 x_2 - x_1^2}{r^2} = 0 \quad \text{as } x_1 = 0 \quad (\text{A.8})$$

$$w_i = \frac{x_i x_{i+1} - x_{i-1} x_i}{r^2} \quad (\text{A.9})$$

$$w_P = \frac{x_P^2 - x_{P-1} x_P}{r^2} \quad (\text{A.10})$$

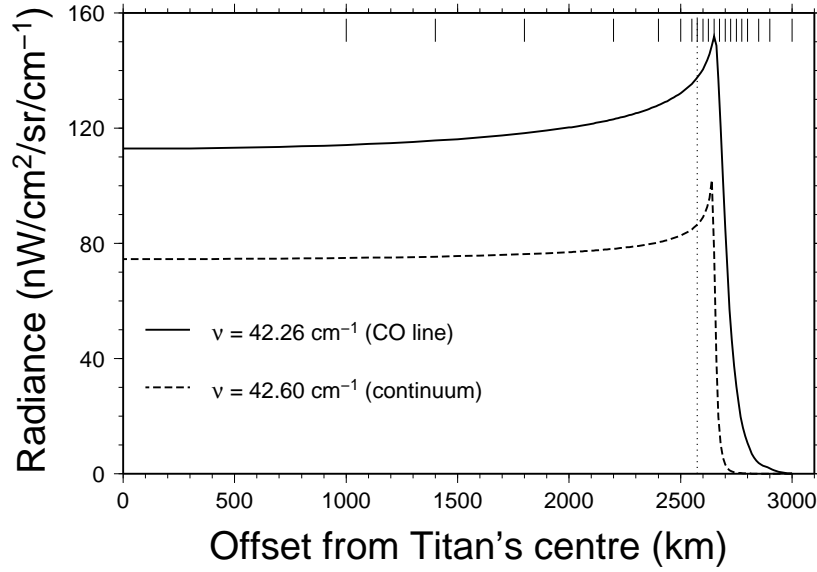


Figure A.10: Line and continuum spectral radiance profiles as a function of offset from Titan's centre. Significant emission takes place beyond the solid body radius at 2575 km. Vertical ticks indicate the location of FOV averaging points used to calculate the disc-averaged spectral radiance. Smaller spacing is required near the limb to capture the limb brightening effects.

694 We found that 21 field of view averaging points were sufficient to accu-
695 rately model the disc-averaged spectrum to within the measurement error.
696 These points and their weights are given in Table A.3.

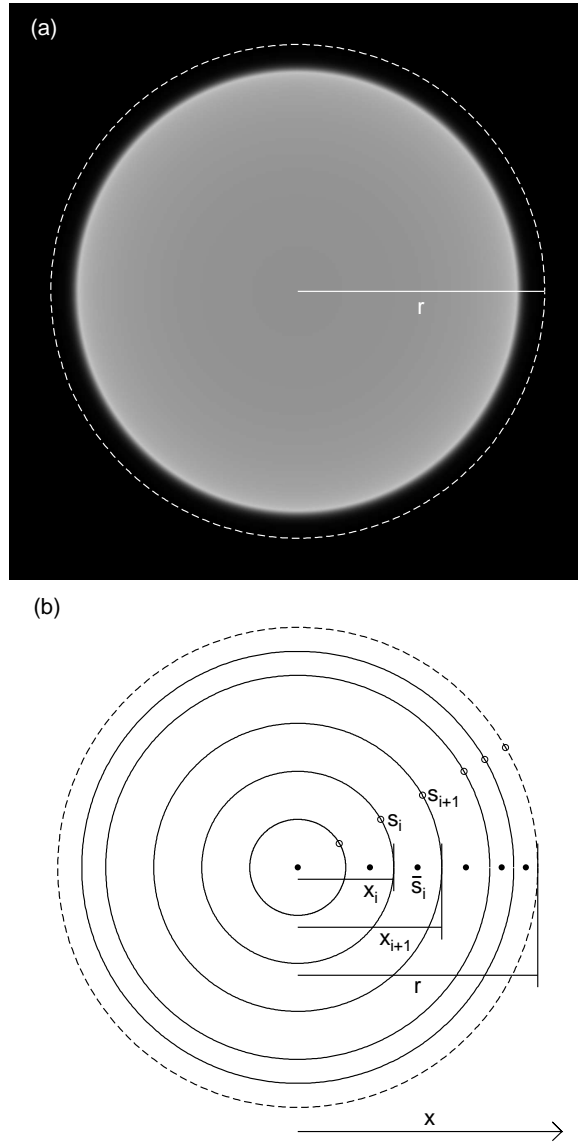


Figure A.11: (a) Synthetic image of Titan created using the CO line emission at 42.26 cm^{-1} in Figure A.10. Limb brightening is evident and emission drops to zero for $x > r$. Dashed line show $r=3000 \text{ km}$. The SSW field of view is very large and subtends $11\text{-}19''$ compared to Titan's $0.7''$ diameter, so is not shown. (b) Illustration of terminology used to define the disc-averaged spectral radiance. Titan is split into 21 unequal annuli with radii between 0 and $r=3000 \text{ km}$.

i	x (km)	Tangent Alt. (km)	Emission Angle (°)	w_i
1	0	-	0.0	0.0
2	1000	-	22.85	0.15556
3	1400	-	32.94	0.12444
4	1800	-	44.35	0.16000
5	2200	-	58.69	0.14667
6	2400	-	68.75	0.08000
7	2500	-	76.14	0.04167
8	2550	-	82.01	0.02125
9	2575	0	90	0.01431
10	2600	25	90	0.01444
11	2625	50	90	0.01458
12	2650	75	90	0.01472
13	2675	100	90	0.01486
14	2700	125	90	0.01500
15	2725	150	90	0.01514
16	2750	175	90	0.01528
17	2775	200	90	0.01542
18	2800	225	90	0.02333
19	2850	275	90	0.03167
20	2900	325	90	0.04833
21	3000	425	90	0.03333

Table A.3: Field of view averaging points used to produce the synthetic reference spectra.
The weights w_i add up to unity.